# Supporting Information

**Fibrous Strain Sensor with Ultra-sensitivity, Wide Sensing Range, and Large Linearity for Full-Range Detection of Human Motion**

*Hanguang Wu, Qiang Liu, Hongwu Chen, Gaoquan Shi, and Chun Li**

Dr. H. G. Wu, Q. Liu, Dr. W. C. Du, Prof. G. Q. Shi, Dr. C. Li,

Department of Chemistry, MOE Key Laboratory of Bioorganic Phosphorus Chemistry & Chemical Biology, Tsinghua University, Beijing 100084, People's Republic of China.

* E-mail:: chunli@mail.tsinghua.edu.cn

## 1. Supplementary Table

**Table S1** The performance comparison of strain sensors

| Resistive-type strain sensors | Maximum sensing range | Limit of detection | Average gauge factor | Reference |
|---|---|---|---|---|
| FPC strain sensor | 150% | 0.1% | 80-350 | This paper |
| Fragmentized graphene foam based sensor | 70% | 0.08% | 29 | S1 |
| Carbonized cotton fabric based sensor | 140% | 0.02% | 64 | S2 |
| graphene-based fiber with “compression spring” architecture | 200% | 0.2% | 3.5 | S3 |
| Multilayered Au nanosheet films based sensor | 70% | a | 36 | S4 |
| ultrathin CPC layer-decorated PU yarn based sensor | 1% | 0.1% | 39 | S5 |
| Parallel micro-cracked graphite film-based sensor | 50% | 0.5% | 500 | S6 |
| Silver nanowire elastomer nanocomposite based sensor | 70% | a | 8 | S7 |
| Carbon nanotubes-Ecoflex nanocomposites based sensor | 500% | a | 2 | S8 |
| Aligned single-walled carbon nanotubes based sensor | 300% | a | 1 | S9 |
| ZnO nanowire/Polystyrene hybridized film based sensor | 50% | 1.5% | 120 | S10 |
| Embedded 3D printing sensor | 400% | a | 5 | S11 |
| Graphene/natural rubber composite based sensor | 800% | a | 32 | S12 |
| Nanoscale cracked Pt/PET film | 2% | 0.5% | 2000 | S13 |
| AuNWs/PANI film based sensor | 100% | a | 20.4-61.4 | S14 |
| AgNWs-PEDOT:PSS/PU nanocomposite sensor | 100% | 1.5% | 1.07-12.4 | S15 |
| AuNWs/Latex rubber film based sensor | 350% | 0.5% | 6.9-9.9 | S16 |
| CNT/PEDOT:PSS/PU nanohybrid based sensor | 100% | a | 8.7-62.3 | S17 |
| Graphene nanoplatelets coated yarn based sensor | 150% | a | 2 | S18 |
| Graphene-nanocellulose paper based sensor | 100% | 6% | 8 | S19 |
| Graphene mesh fabric on stretchable tape | 7.5% | a | 20 | S20 |
| Fabricated by pencil drawn | 0.6% | 0.13% | 536.6 | S21 |
| Laser scribed graphene on PDMS | 10% | a | 9.5 | S22 |
| Fish scale-like rGO/tape film | 82% | 0.1% | 16.2 | S23 |

**Table S2** The *GF* values of FPC strain sensors integrated into the sensing fabric and the resistance variation during clenching and "victory" gesture (X and Y are designed according to Fig. S12)

| | Measured *GF* | Clenching | | "Victory" Gesture | |
|---|---|---|---|---|---|
| | | $\Delta R/R_0$ | Calculated Strain (%) | $\Delta R/R_0$ | Calculated Strain (%) |
| $\mathbf{X_{11}}$ | 75 | 1.27 | 1.7 | 1.22 | 1.63 |
| $\mathbf{X_{12}}$ | 67 | 0.94 | 1.4 | 0.95 | 1.42 |
| $\mathbf{X_{13}}$ | 76.4 | 0.81 | 1.06 | 0.31 | 0.41 |
| $\mathbf{X_{21}}$ | 63 | 0.68 | 1.08 | 0.39 | 0.62 |
| $\mathbf{X_{22}}$ | 82 | 0.67 | 0.82 | 0.34 | 0.42 |
| $\mathbf{X_{23}}$ | 71 | 0.78 | 1.1 | 0.05 | 0.07 |
| $\mathbf{X_{31}}$ | 74 | 0.67 | 0.91 | 0.27 | 0.37 |
| $\mathbf{X_{32}}$ | 86 | 0.63 | 0.73 | 0.086 | 0.1 |
| $\mathbf{X_{33}}$ | 78 | 0.77 | 0.99 | 0.04 | 0.05 |
| $\mathbf{Y_{11}}$ | 69 | 2.5 | 3.6 | 1.66 | 2.4 |
| $\mathbf{Y_{12}}$ | 71 | 2.7 | 3.8 | 0.327 | 0.46 |
| $\mathbf{Y_{13}}$ | 70 | 2.59 | 3.7 | 0.006 | 0.009 |
| $\mathbf{Y_{21}}$ | 76 | 2.2 | 2.9 | 1.39 | 1.83 |
| $\mathbf{Y_{22}}$ | 67 | 2.08 | 3.1 | 0.35 | 0.52 |
| $\mathbf{Y_{23}}$ | 78 | 1.87 | 2.4 | 0.009 | 0.012 |
| $\mathbf{Y_{31}}$ | 76 | 1.6 | 2.1 | 1.14 | 1.5 |
| $\mathbf{Y_{32}}$ | 73 | 1.6 | 2.2 | 0.08 | 0.11 |
| $\mathbf{Y_{33}}$ | 83 | 1.33 | 1.6 | 0.002 | 0.003 |

## 2. Supplementary Figures

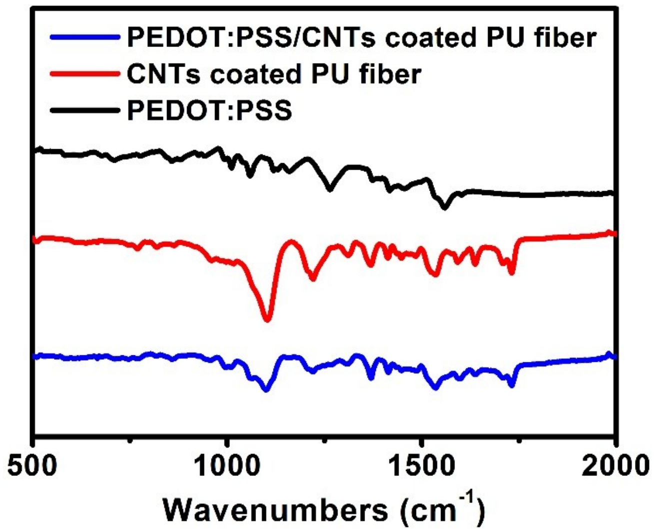


**Fig. S1** IR spectra of PEDOT:PSS, CNTs coated PU fiber, and PEDOT:PSS/CNTs coated PU fiber

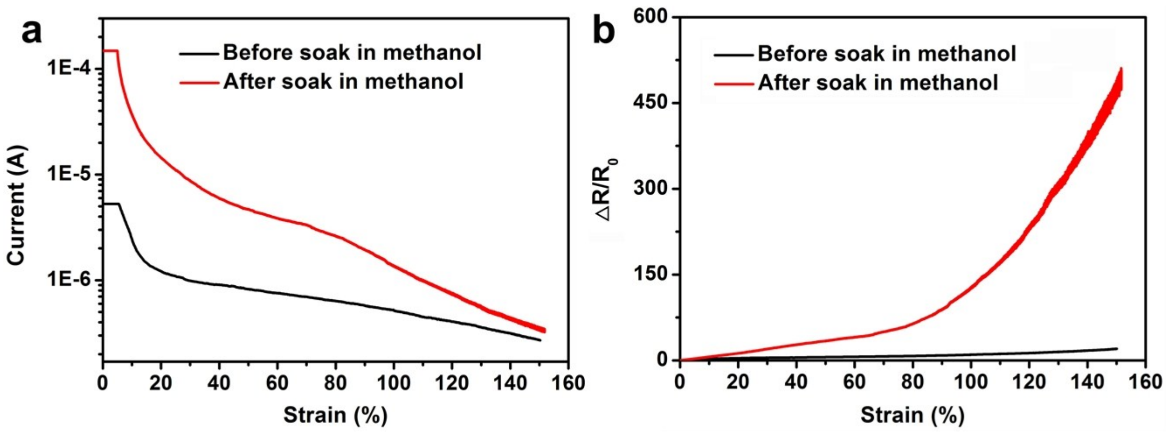


**Fig. S2** (a) Variation of current with strain of FPC strain sensors before and after the treat by methanol. (b) Relative resistance performance of FPC strain sensors before and after the treat by methanol.

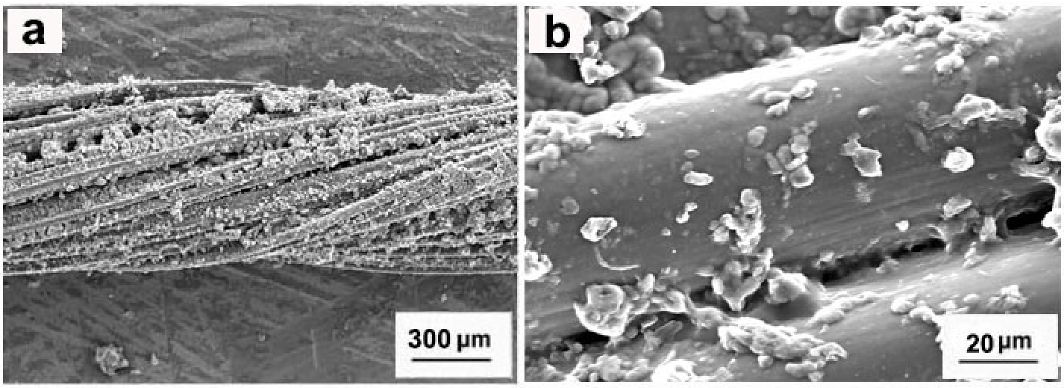


**Fig. S3** (a) SEM image of PEDOT:PSS/CNTs coated PU fiber core substrate; (b) magnified SEM image of PEDOT:PSS/CNTs coated PU fiber core substrate: the bottom of CNTs agglomerates are covered and fixed by the PEDOT:PSS layer.

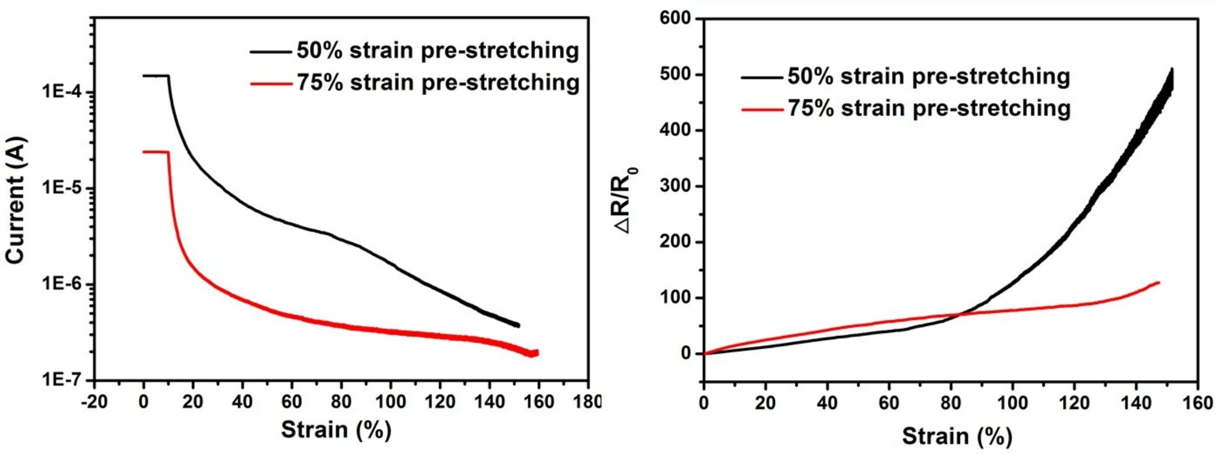


**Fig. S4** (a) Variation of current with strain of FPC strain sensors with 50% elongation of pre-stretching. (b) Relative resistance performance of FPC strain sensors with 75% elongation of pre-stretching.

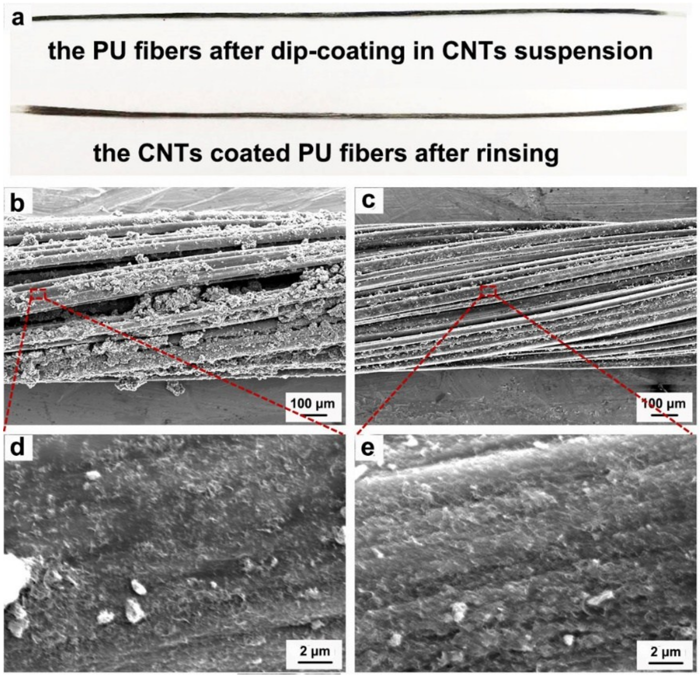


**Fig. S5** (a) Comparison of the morphologies of PU fiber cores with and without attachment of CNTs agglomerates. (b) SEM image of PU fiber cores with CNTs agglomerates. (c) SEM image of PU fiber cores without CNTs agglomerates. (d) Magnified SEM image of PU fiber cores with CNTs agglomerates. (e) Magnified SEM image of PU fiber cores without CNTs agglomerates.

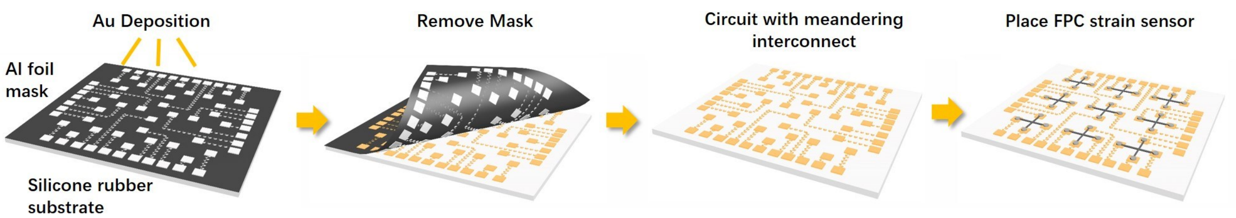


**Fig. S6** Fabrication process of the multi-pixel sensor array based on the FPC atrain sensors

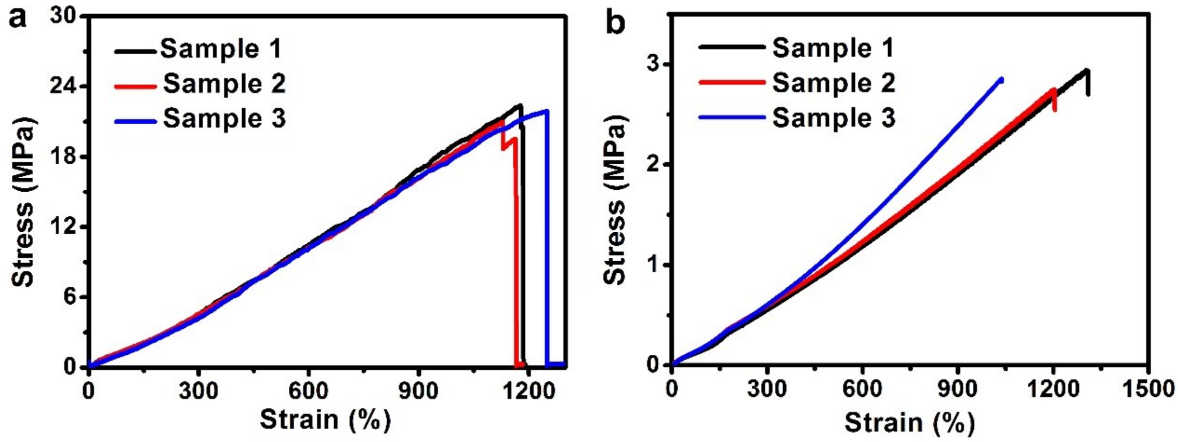


**Fig. S7** Mechanical behavior of (a) PU fiber; (b) Dragon Skin elastomer

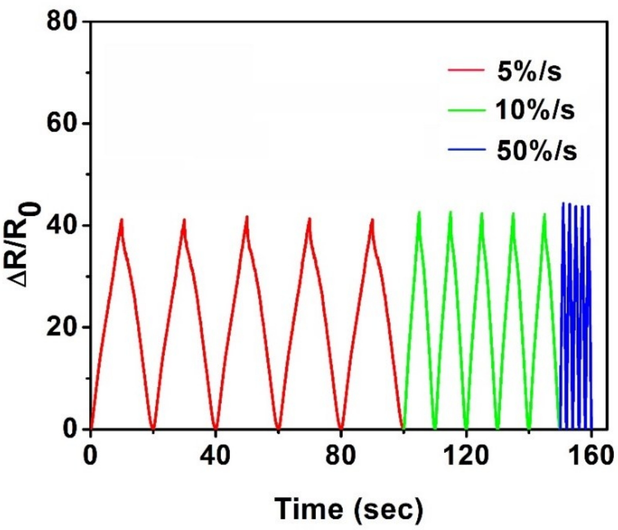


**Fig. S8** Variations of relative resistance of FPC strain sensor during the stretching-releasing process for 50% at the rate of 5% $s^{-1}$, 10% $s^{-1}$, 50% $s^{-1}$, respectively.

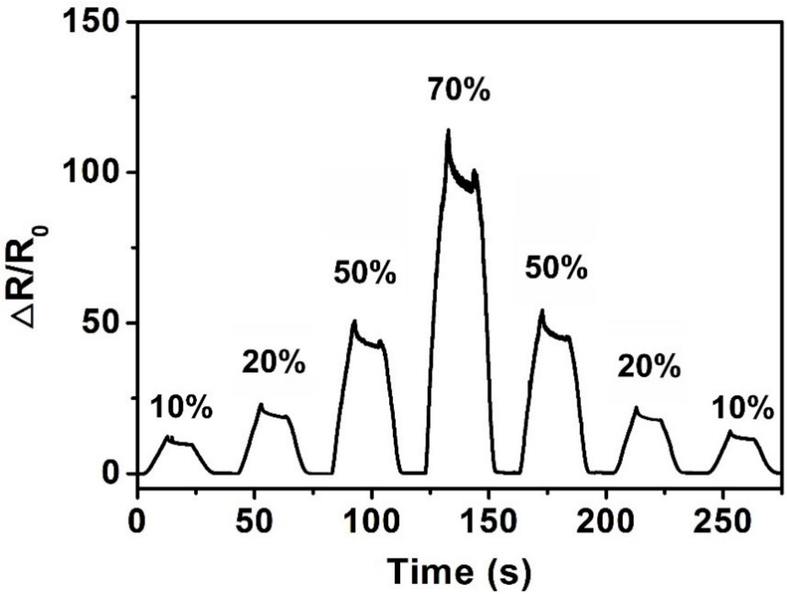


**Fig. S9** Relative resistance response of the strain sensor to different strains after a stepped strain change.

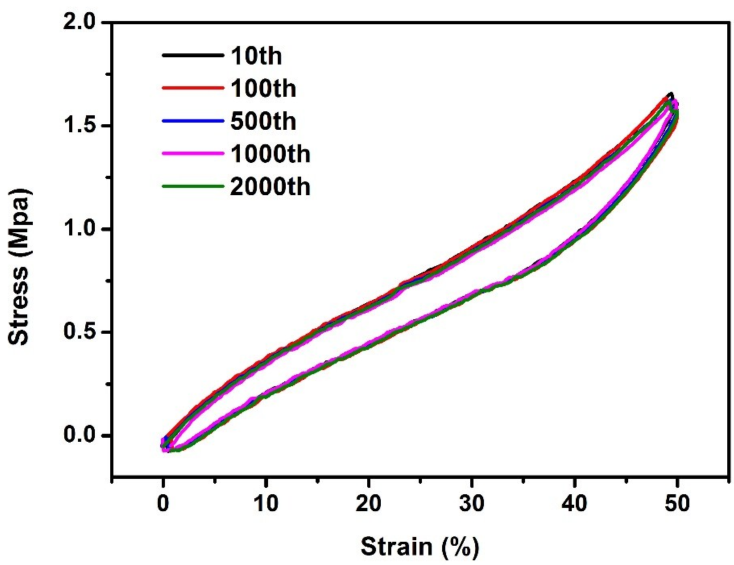


**Fig. S10** Mechanical stability of the PEDOT:PSS-CNTs/PU composite fiber upon cyclic stretching/releasing to 50% for 2000 cycles.

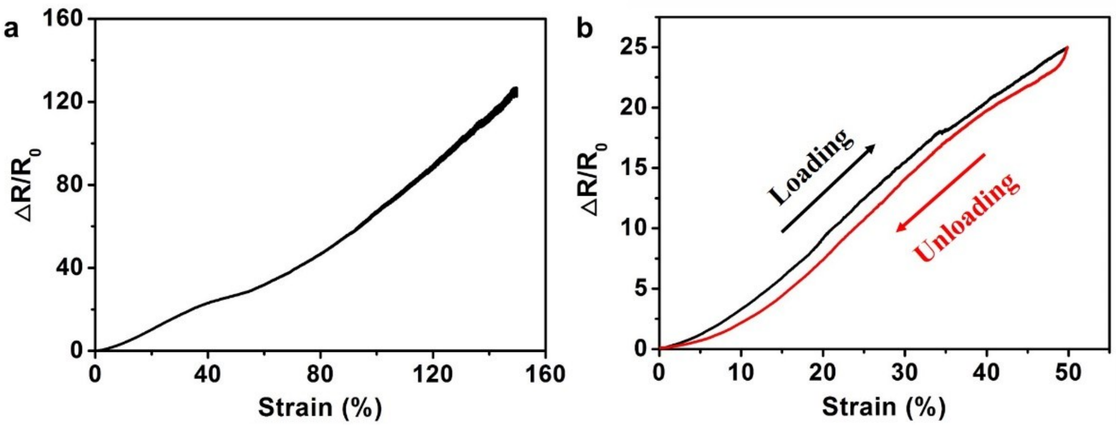


**Fig. S11** Electromechanical behaviors of the fibrous strain sensor with only CNTs as the sensing layer. (a) $\Delta R/R_0$-ε curve of the sensor recorded at a stretching rate of 1% $sec^{-1}$. (b)Variation in $\Delta R/R_0$ of the sensor under a 50% strain loading-unloading cycle.

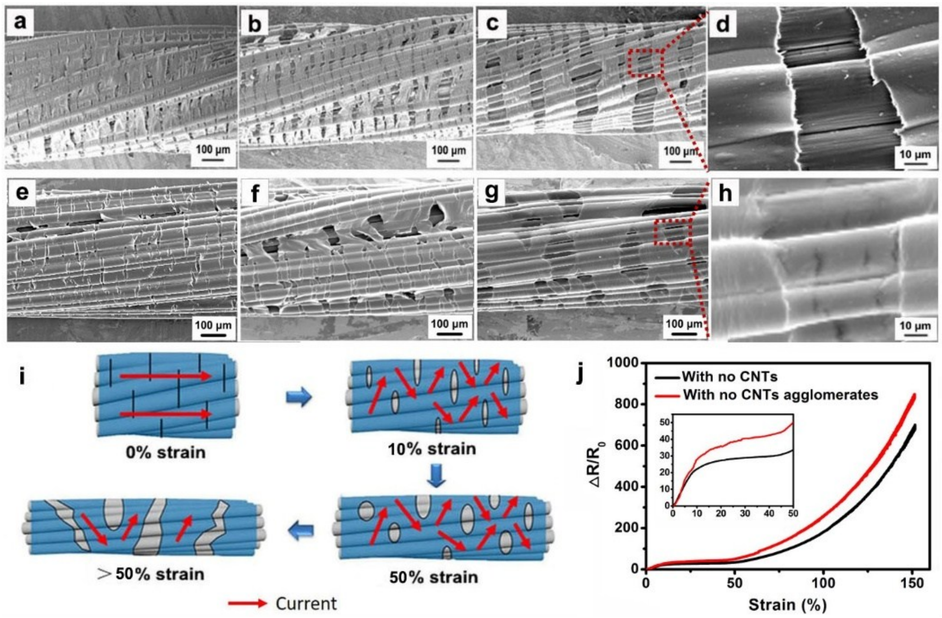


**Fig. S12** SEM image of the fibrous strain sensor without addition of CNTs at (a) 0% strain. (b) 30% strain. (c) 70% strain. (d) Magnified SEM image of the fibrous strain sensor without addition of CNTs at 70% strain. SEM image of the fibrous strain sensor without CNTs agglomerates at (e) 0% strain. (f) 30% strain. (g) 70% strain. (h) Magnified SEM image of the fibrous strain sensor without CNTs agglomerates at 70% strain. (i) Schematic illustration of the fibrous strain sensor without CNTs agglomerates upon stretching. (j) $\Delta R/R_0$ - $\varepsilon$ curves of fibrous strain sensors with no CNTs and without CNTs agglomerates. The inset reproduces the curves within 0-50% strain range.

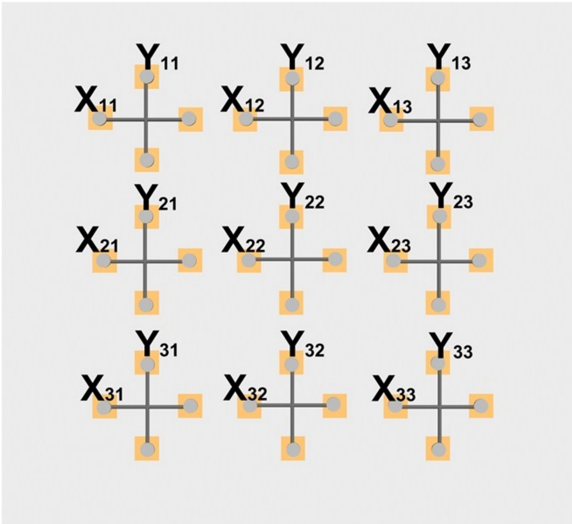


**Fig. S13** FPC strain sensors integrated on the electronic fabric with 3 × 3 pixel array

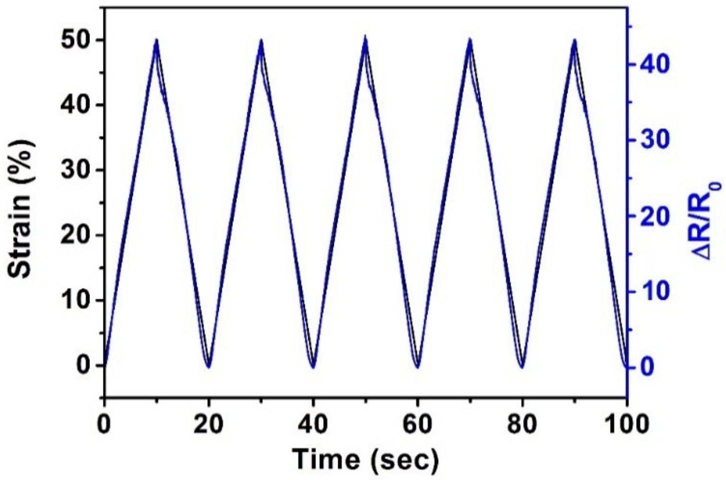


**Fig. S14** Cycling test of FPC strain sensor at a stretching/releasing rate of 1% $s^{-1}$; its relative resistance changes synchronously with strain.

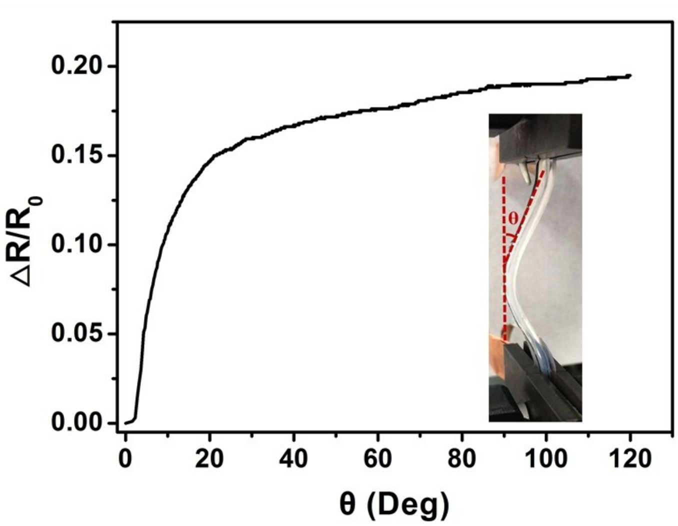


**Fig. S15** Plot of relative resistance as a function of bending degree. Inset: FPH strain sensor in bending testing.

## 3. Simulation of the sensing mechanism

Based on the microstructure variation of the FPC strain sensor, the resistance variation of the strain sensor was simplified into a network circuit model (Fig. 3d). In this model, total resistance of the sensor consists of the resistance of the PEDOT:PSS fragments wrapped on each PU fibers ($R_1$, $R_2$… $R_x$, $R_1$', $R_2$'… in Fig. 3d) and the contact resistance between PEDOT:PSS fragments and CNTs agglomerates ($R_c$ in Fig. 3d). During uniaxial stretching, the resistance of every PEDOT:PSS fragments are approximated to be constant, and the increase in the resistance of the sensor is mainly attributed to the change of $R_c$. We simplified the change in $R_c$ as the result of the stochastic break of the conductive path, and the proportion of the break is proportional to the strain.

By inputting the model into NI Multisim$^{TM}$, the currents of the circuit with a specified proportional of the break can be calculated (spots in Fig. 3e). Based on our assumption that the proportion of break is proportional to the strain, the variation of current with extensional strain can be simulated. Thus, the change of the $\Delta R/R_0$ with the strain ($\varepsilon$) is simulated, and fitted by using $\Delta R/R_0$ - $\varepsilon$ curves, as shown in Fig. 3e. Through changing the number of the conductive path (n in Fig. 3d), the $\Delta R/R_0$ - $\varepsilon$ curves of the FPC strain sensor with different PU fibers (m in Fig. 3d) can be obtained.

The simulated results show that the sensing architecture of FPC strain sensors will provide a good linear relationship between $\Delta R/R_0$ and $\varepsilon$ at low strain, consistent well with the experimental results (Fig. 2d). However, this linear relationship will be terminated with the increase in the extensional strain, especially for the sensors with less PU fibers. In addition, the simulated curves show that *GF* (the slopes of $\Delta R/R_0$ - $\varepsilon$ curves) increases with the decrease of the PU fibers, consistent well with the experimental results in Fig. 2a. This could be attributed to the stronger influence of a quantitative break in the whole conductive network.

**Supplementary References**


S1 Y. R. Jeong, H. Park, S. W. Jin, S. Y. Hong, S. S. Lee, J. S. Ha, *Adv. Funct. Mater.* **2015**, *25*, 4228.

S2 M. Zhang, C. Wang, H. Wang, M. Jian, X. Hao, Y. Zhang, *Adv. Funct. Mater.* **2017**, *27*, 1604795.

S3 Y. Cheng, R. Wang, J. Sun, L. Gao, *Adv. Mater.* **2015**, *27*, 7365.

S4 G.-H. Lim, N.-E. Lee, B. Lim, *J. Mater. Chem. C* **2016**, *4*, 5642.

S5 X. Wu, Y. Han, X. Zhang, C. Lu, *ACS Appl. Mater. Interfaces* **2016**, *8*, 9936.

S6 M. Amjadi, M. Turan, C. P. Clementson, M. Sitti, *ACS Appl. Mater. Interfaces* **2016**, *8*, 5618.

S7 M. Amjadi, A. Pichitpajongkit, S. Lee, S. Ryu, I. Park, *ACS Nano* **2014**, *8*, 5154.

S8 M. Amjadi, Y. J. Yoon, I. Park, *Nanotechnology* **2015**, *26*, 375501.

S9 T. Yamada, Y. Hayamizu, Y. Yamamoto, Y. Yomogida, A. Izadi-Najafabadi, D. N. Futaba, K. Hata, *Nat. Nanotechnol.* **2011**, *6*, 296.

S10 X. Xiao, L. Yuan, J. Zhong, T. Ding, Y. Liu, Z. Cai, Y. Rong, H. Han, J. Zhou, Z. L. Wang, *Adv. Mater.* **2011**, *23*, 5440.

S11 J. T. Muth, D. M. Vogt, R. L. Truby, Y. Mengüç, D. B. Kolesky, R. J. Wood, J. A. Lewis, *Adv. Mater.* **2014**, *26*, 6307.

S12 C. S. Boland, U. Khan, C. Backes, A. O'Neill, J. McCauley, S. Duane, R. Shanker, Y. Liu, I. Jurewicz, A. B. Dalton, *ACS Nano* **2014**, *8*, 8819.

S13 D. Kang, P. V. Pikhitsa, Y. W. Choi, C. Lee, S. S. Shin, L. Piao, B. Park, K.-Y. Suh, T.-i. Kim, M. Choi, *Nature* **2014**, *516*, 222.

S14 S. Gong, D. T. Lai, Y. Wang, L. W. Yap, K. J. Si, Q. Shi, N. N. Jason, T. Sridhar, H. Uddin, W. Cheng, *ACS Appl. Mater. Interfaces* **2015**, *7*, 19700.

S15 J.-H. Lee, B.-U. Hwang, T. Q. Trung, E. Roh, D.-I. Kim, S.-W. Kim, N.-E. Lee, *ACS Nano* **2015**, *9*, 8801.

S16 S. Gong, D. T. H. Lai, B. Su, K. J. Si, Z. Ma, L. W. Yap, P. Guo, W. Cheng, *Adv. Electron. Mater.* **2015**, *1*, 1400063.

S17 E. Roh, B.-U. Hwang, D. Kim, B.-Y. Kim, N.-E. Lee, *ACS Nano* **2015**, *9*, 6252.

S18 J. J. Park, W. J. Hyun, S. C. Mun, Y. T. Park, O. O. Park, *ACS Appl. Mater. Interfaces* **2015**, *7*, 6317.

S19 C. Yan, J. Wang, W. Kang, M. Cui, X. Wang, C. Y. Foo, K. J. Chee, P. S. Lee, *Adv. Mater.* **2014**, *26*, 2022.

S20 Q. Liu, M. Zhang, L. Huang, Y. Li, J. Chen, C. Li, G. Shi, *ACS Nano* **2015**, *9*, 12320.

S21 X. Liao, Q. Liao, X. Yan, Q. Liang, H. Si, M. Li, H. Wu, S. Cao, Y. Zhang, *Adv. Funct. Mater.* **2015**, *25*, 2395.

S22 H. Tian, Y. Shu, Y.-L. Cui, W.-T. Mi, Y. Yang, D. Xie, T.-L. Ren, *Nanoscale* **2014**, *6*, 699.

S23 Q. Liu, J. Chen, Y. Li, G. Shi, *ACS Nano* **2016**, *10*, 7901.